

See discussions, stats, and author profiles for this publication at: <https://www.researchgate.net/publication/26812018>

# Strong Polarization Dependence of Plasmon-Enhanced Fluorescence on Single Gold Nanorods

ARTICLE *in* NANO LETTERS · SEPTEMBER 2009

Impact Factor: 13.59 · DOI: 10.1021/nl902095q · Source: PubMed

---

CITATIONS

161

---

READS

231

7 AUTHORS, INCLUDING:



**Tian Ming**

Massachusetts Institute of Technology

40 PUBLICATIONS 1,698 CITATIONS

SEE PROFILE



**Lei Zhao**

Nanjing University

95 PUBLICATIONS 859 CITATIONS

SEE PROFILE

# Strong Polarization Dependence of Plasmon-Enhanced Fluorescence on Single Gold Nanorods

Tian Ming,<sup>†</sup> Lei Zhao,<sup>†</sup> Zhi Yang,<sup>†</sup> Huanjun Chen,<sup>†</sup> Lingdong Sun,<sup>‡</sup>  
Jianfang Wang,<sup>\*,†</sup> and Chunhua Yan<sup>‡</sup>

*Department of Physics, the Chinese University of Hong Kong, Shatin, Hong Kong  
SAR, and State Key Lab of Rare Earth Materials Chemistry and Applications, Peking  
University, Beijing 100871, China*

*Received July 1, 2009; Revised Manuscript Received August 30, 2009*

## ABSTRACT

We report on the strong polarization dependence of the plasmon-enhanced fluorescence on single gold nanorods. The fluorescence from the organic fluorophores that are embedded in a mesostructured silica shell around individual gold nanorods is enhanced by the longitudinal plasmon resonance of the nanorods. Our electrostatic calculations show that under an off-resonance excitation, the electric field intensity contour around a nanorod rotates away from the length axis as the excitation polarization is varied. The polarization dependence of the plasmon-enhanced fluorescence is ascribed to the dependence of the averaged electric field intensity enhancement within the silica shell on the excitation polarization. The measured fluorescence enhancement factor is in very good agreement with that obtained from the electrostatic calculations. The fluorescence enhancement factor increases as the longitudinal plasmon wavelength is synthetically tuned close to the excitation wavelength. In addition, the polarization dependence is used to determine the orientation angle of the gold nanorods. The results are in excellent agreement with the actual measurements. Furthermore, the emission spectrum of the fluorophore is modified by the longitudinal plasmon resonance of the gold nanorods. A linear correlation between the emission peak wavelength and the longitudinal plasmon wavelength is obtained.

Noble metal nanocrystals exhibit extraordinary plasmonic properties. The excitation of their localized surface plasmon resonance modes results in the confinement of electromagnetic waves in regions below the diffraction limit near the metal surface. This near-field enhancement has been employed to amplify Raman scattering,<sup>1</sup> fluorescence,<sup>2–8</sup> high-harmonic generation,<sup>9</sup> Faraday rotation,<sup>10</sup> photocurrent,<sup>11</sup> photopolymerization,<sup>12</sup> light absorption,<sup>13</sup> and circular dichroism.<sup>14</sup> On the other hand, the localized plasmon modes of elongated metal nanocrystals are inherently anisotropic.<sup>15–19</sup> The optical signal amplification is therefore expected to be strongly dependent on the excitation polarization direction. Up to date, polarization-dependent amplification has been mainly observed in Raman scattering from dimers and trimers of metal nanocrystals assembled on substrates.<sup>20–25</sup> Here, we report on the high polarization dependence of the fluorescence enhancement on single Au nanorods on the basis of the successful fabrication of hybrid nanostructures composed of Au nanorod cores and fluorophore-doped mesostructured silica shells. Our finite-difference time-domain (FDTD)

calculations show that the polarization dependence is ascribed to the dependence of the averaged electric field intensity enhancement within the silica shell on the excitation polarization. We demonstrate the determination of the orientation of the Au nanorods on substrates and the variation of the fluorescence enhancement factor with the plasmon wavelength of the Au nanorods, as well as the shaping of the emission spectrum of the fluorophore.

The hybrid nanostructures, which are schematically shown in Figure 1a, were fabricated by coating a mesostructured silica shell onto each Au nanorod. The Au nanorods were grown in aqueous solutions using a seed-mediated method. The growth followed the procedure reported previously by us.<sup>26</sup> The longitudinal plasmon resonance wavelengths of the Au nanorods were finely tailored through an anisotropic oxidation reaction.<sup>27</sup> The particle concentrations of the obtained Au nanorods were estimated to be 0.13 nM. The as-grown Au nanorods are encapsulated with cetyltrimethylammonium bromide (CTAB) surfactant, which makes the nanorods positively charged. The encapsulating CTAB surfactant can function as a structure-directing agent and therefore facilitate the formation of a mesostructured silica shell around the Au nanorods. Oxazine 725 perchlorate (Figure 1b and Figure S1 in Supporting Information) was

\* To whom correspondence should be addressed. E-mail: jfwang@phy.cuhk.edu.hk. Tel: +852 3163 4167. Fax: +852 2603 5204.

<sup>†</sup> The Chinese University of Hong Kong.

<sup>‡</sup> Peking University.

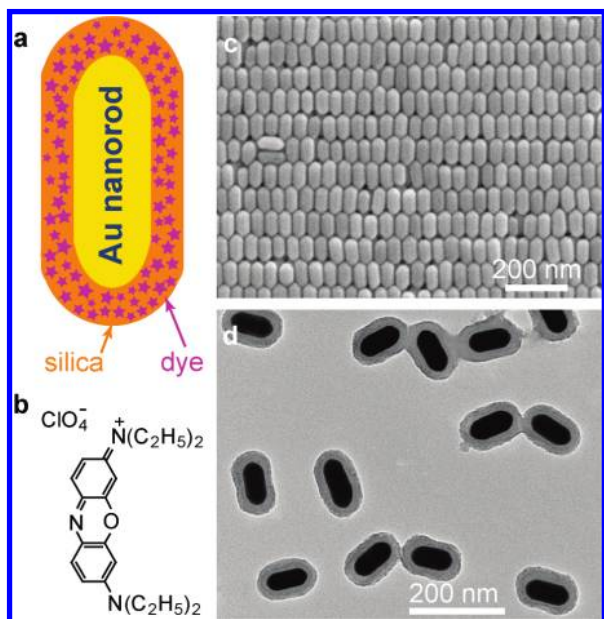


**Figure 1.** Hybrid nanostructures: (a) schematic illustration; (b) molecular structure of oxazine 725; (c) SEM image of bare Au nanorods; (d) TEM image of the core–shell nanostructures. Each nanostructure is composed of a single Au nanorod core and a dye-incorporated mesostructured silica shell.

chosen for the fabrication of the Au nanorod–fluorophore hybrid nanostructures. The preparation procedure was modified from that developed for coating mesostructured silica shells on CTAB-stabilized inorganic nanocrystals.<sup>28</sup> The incorporation of oxazine 725 into the silica shell was realized simply by dissolving the dye molecules in the silica precursor solution.<sup>29</sup> Specifically, 3 mL of the as-prepared Au nanorod dispersion was centrifuged at 6000 rpm for 10 min to remove excess CTAB surfactants. The precipitate was redispersed in 2 mL of deionized water. Twenty microliters of an aqueous solution of oxazine 725, which was made by dissolving 2.3 mg of oxazine 725 perchlorate in 200  $\mu$ L of water with ultrasonication, and 20  $\mu$ L of a 0.1 M aqueous NaOH solution were then added under vigorous stirring. After this step, three 12  $\mu$ L injections of 20 vol % tetraethyl orthosilicate in methanol were carried out under gentle stirring at 60 min intervals. After the mixture was allowed to react for 14 h, the resultant hybrid nanostructures were washed by two cycles of centrifugation and redispersion in water at the same volume. The hybrid nanostructures were deposited on 0.2 mm thick cleaned glass slides by immersing the slides in the obtained nanostructure dispersion for 5 min and then blowing them dry with nitrogen.

Panels c and d of Figure 1 show representative scanning electron microscopy (SEM, FEI Quanta 400 FEG) and transmission electron microscopy (TEM, FEI CM120) images of a nanorod sample before and after silica coating, respectively. The average length, diameter, and aspect ratio of the bare nanorods are  $89 \pm 7$  nm,  $42 \pm 3$  nm, and  $2.1 \pm 0.2$ , respectively. The ensemble longitudinal plasmon wavelength is 646 nm when the nanorods are dispersed in aqueous solutions. The silica shell thickness is uniform around the nanorod, with an average value of  $21 \pm 2$  nm. The concentration of oxazine 725 in the silica shell is estimated

to be 11 molecules per 1000 nm<sup>3</sup>. There are totally  $\sim 5400$  molecules in the entire silica shell. The Au nanorods with other longitudinal plasmon wavelengths in the range of 590–810 nm were also prepared (Figure S2 in Supporting Information). After silica coating, their longitudinal plasmon peaks are red-shifted by 10–30 nm, owing to the increase in the refractive index of the surrounding medium.

The Au nanorod–fluorophore hybrid nanostructures were deposited on glass slides at a surface number density of  $\sim 2300$  mm<sup>−2</sup>. The nanostructures were first subjected to fluorescence and dark-field measurements. Single-particle dark-field scattering and fluorescence measurements were performed on an upright Olympus BX60 optical microscope integrated with an Acton SpectraPro 2300i monochromator and a Princeton Instruments Pixis 512B charge-coupled device, which was thermoelectrically cooled to  $-50$  °C. Both the scattering and fluorescence signals were collected with an Olympus LMPlanFI dark-field objective (50 $\times$ , NA 0.50) and focused onto the entrance slit of the monochromator for imaging and spectroscopy. A 100 W quartz–tungsten–halogen lamp was employed as the white light source for scattering measurements. The scattering spectra from single particles were corrected by subtracting background spectra taken from the nearby regions containing no particles. A Thorlabs HeNe laser (633 nm, 5.0 mW) was used as the excitation source for fluorescence measurements. The laser light was introduced sideways to the bottom side of the glass slide at a surface power density of 0.7 mW·cm<sup>−2</sup>. A Soleil Babinet compensator adjusted to function as a half-wave plate for the 633 nm laser light was employed to vary the excitation polarization direction. A long-pass 647 nm edge filter was placed in front of the monochromator to block the excitation light during fluorescence measurements. After the optical measurements, the nanostructures were sputter-coated (Polaron SC502 sputter coater) with gold for SEM imaging. The same nanostructures that measured optically were located under SEM imaging by a pattern-matching method. Panels a and b of Figure 2 show the SEM and scattering image from the same region containing seven nanostructures, which are from the same sample as shown in Figure 1d. The distribution patterns in both images show a perfect match. After the nanostructures were imaged under the dark-field mode, the optical system was switched to the fluorescence mode. The fluorescence images were taken consecutively as the excitation polarization angle was varied at 10° per step. The fluorescence intensity of each nanostructure is seen to change systematically as a function of the excitation polarization angle. The intensity variations are out of phase for different nanostructures (video S1, Supporting Information). Panels c and d of Figure 2 show two representative fluorescence images acquired with the excitation polarizations perpendicular to each other.

Each emission spot on the fluorescence images was fitted with a two-dimensional Gaussian peak (Figure S3 in Supporting Information). The peak value was taken as the fluorescence intensity. Figure 2e shows the plot of the fluorescence intensity versus the excitation polarization angle for the nanostructure 4. The intensity varies periodically and

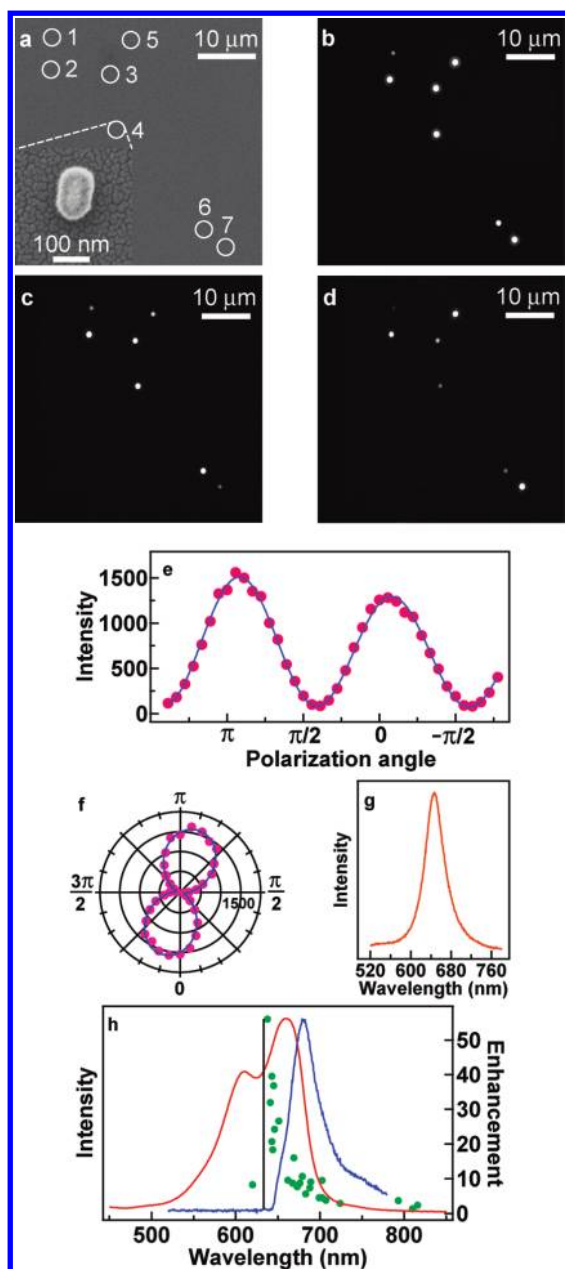


**Figure 2.** Polarization dependence of the fluorescence from individual hybrid nanostructures. (a) SEM image. The nanostructures are indicated by circles, with the nanostructure 4 enlarged in the inset. (b) Scattering image. (c, d) Fluorescence images obtained with the excitation polarizations perpendicular to each other. (e) Dependence of the fluorescence intensity on the excitation polarization angle (solid red circles) for the nanostructure 4 shown in (a). The blue curve is a fit to a cosine squared function together with an exponential decay (see below). (f) Polar plot of the fluorescence intensity (solid red circles) versus the excitation polarization direction. The blue curve is a fit to the cosine squared function without the exponential decay. (g) Scattering spectrum of the nanostructure 4. (h) Dependence of the fluorescence enhancement (solid green circles, right axis) on the longitudinal plasmon wavelength. The Au nanorods with varying longitudinal plasmon wavelengths were prepared for this measurement. The red curve is the absorption spectrum (left axis) of oxazine 725 embedded in mesostructured silica, acquired on a Hitachi U-3501 UV–visible–NIR spectrophotometer. The blue curve is the fluorescence emission spectrum (left axis) of oxazine 725 acquired from the nanostructure 4, with the left side cutoff by the long-pass filter. The excitation wavelength is indicated by the solid black line.

can be fitted using a cosine squared function together with an exponential decay (see below). The intensity decay is caused by laser-induced photobleaching. The polarization dependence is also shown clearly by a dipole-like pattern in the polar plot (Figure 2f). Because the longitudinal plasmon mode of Au nanorods is inherently polarized along the nanorod length axis,<sup>15,17,19</sup> it will be excited when the excitation is polarized along the length axis and remain unexcited when the excitation is polarized perpendicular to the length axis. In addition, because the fluorescence enhancement of fluorophores results from the plasmon-induced increases in the near-field excitation rate and the radiative decay rate,<sup>3–8,22</sup> the fluorescence enhancement factor can be determined by taking the ratio between the maximum and minimum fluorescence intensities, which correspond to the parallel and perpendicular excitation polarization, respectively. The fluorescence enhancement factor determined in this way for nanostructure 4 is 37.

The dark-field scattering spectra of the hybrid nanostructures were also measured. Figure 2g shows the scattering spectrum of nanostructure 4. The peak arises from the longitudinal plasmon mode. It has a peak wavelength of 647 nm and a full width at half-maximum of 46 nm. The transverse plasmon resonance of the nanostructures is too weak to be detected with the dark-field scattering technique. In addition, the transverse plasmon wavelengths of gold nanorods are relatively insensitive to the nanorod sizes. We therefore in our experiments chose a fluorescent dye with its emission wavelength close to the longitudinal plasmon resonance of the nanorods. By measuring the fluorescence enhancement factors of the hybrid nanostructures with different longitudinal plasmon wavelengths, a relationship between the fluorescence enhancement factor and the longitudinal plasmon wavelength is obtained. Figure 2h shows this relationship, together with the absorption spectrum of oxazine 725 incorporated in mesostructured silica and the fluorescence emission spectrum measured on nanostructure 4. Oxazine 725 exhibits a major absorption peak at 660 nm. The excitation laser wavelength, 633 nm, is on the shoulder of the dye's major absorption peak. The fluorescence enhancement factor is seen to increase rapidly as the longitudinal plasmon wavelength is synthetically tuned toward the excitation laser wavelength by using the Au nanorods with different aspect ratios. A maximum enhancement factor of 56 is obtained when the longitudinal plasmon wavelength is 637 nm.

The longitudinal plasmon mode can not only enhance the fluorescence intensity of oxazine 725 incorporated in the silica shell but also change the spectral shape of its emission. Figure 3a shows five representative scattering spectra of the individual nanostructures and Figure 3b shows the emission spectra of the same nanostructures in corresponding colors. Oxazine 725 is seen to be forced to emit preferentially at the longitudinal plasmon wavelengths of the Au nanorods. The correlation between the emission and the longitudinal plasmon wavelengths shows a linear behavior, with a slope of 0.76 (Figure 3c). This behavior of shaping the emission spectra of fluorophores has recently been observed only on



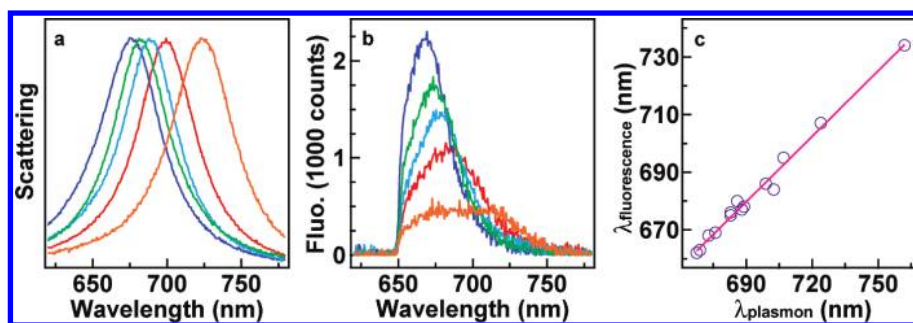


**Figure 3.** Spectral shaping of the emission of oxazine 725. (a) Scattering spectra of the individual hybrid nanostructures containing the Au nanorods with different aspect ratios. (b) Corresponding fluorescence emission spectra. The emission spectra were recorded under the longitudinal polarization excitation. (c) Dependence of the fluorescence peak wavelength (empty circles) of oxazine 725 on the scattering peak wavelength. The line is a linear fit.

plasmon-coupled Au nanoparticles.<sup>30,31</sup> We show that it can also occur on single Au nanorods. The spectral shaping is ascribed to the enhanced probability of the transition of fluorophores from the excited state to a specific vibrational ground state with the transition energy close to the plasmon resonance energy.

FDTD calculations were performed to reveal the electric field intensity contours using FDTD Solutions 6.0, which was developed by Lumerical Solutions, Inc. In the calculation, the Au nanorod is modeled as a cylinder capped with a half sphere at each end. The total length of the nanorod is 93 nm, and the diameter is 43 nm. The thickness of the mesostructured silica shell is 21 nm. These values are nearly the same as the average ones of the sample shown in Figure 1. The Au nanorod–mesostructured silica hybrid nanostructure is surrounded by air. The refractive indices of the silica shell and air are taken to be 1.43 and 1.0, respectively. The dielectric function of gold is represented with a combination of the Drude and Lorentz model

$$\varepsilon_{\text{DL}}(\omega) = \varepsilon_{\infty} - \frac{\omega_{\text{D}}^2}{\omega^2 + i\gamma_{\text{D}}\omega} - \frac{(\Delta\varepsilon)\Omega_{\text{L}}^2}{(\omega^2 - \Omega_{\text{L}}^2) + i\Gamma_{\text{L}}\omega} \quad (1)$$

where the used parameters are the high-frequency dielectric constant  $\varepsilon_{\infty} = 7.0765$ , the plasma frequency  $\omega_{\text{D}} = 13906.9$  THz, the Drude damping constant  $\gamma_{\text{D}} = 14.1084$  MHz, the Lorentz weighting factor  $\Delta\varepsilon = 2.32306$ , the Lorentz oscillator strength  $\Omega_{\text{L}} = 4634.63$  THz, and the Lorentz line width  $\Gamma_{\text{L}} = 926.71$  THz. The entire nanostructure is divided into grids at a size of 0.5 nm. The calculated longitudinal plasmon wavelength is 643 nm with a full width at half-maximum of 40 nm. The corresponding experimental values are 647 and 46 nm, respectively (Figure 2g). There is a very good agreement between the experiment and the calculation. The electric field intensity contours were calculated at the excitation wavelength of 633 nm under different excitation polarization directions. Under this off-resonance excitation, the maximum field enhancement regions are observed to rotate away from the nanorod ends oppositely as the excitation polarization is varied gradually from the longitudinal to transverse directions (Figure 4a). This rotation is ascribed to the phase difference between the longitudinal and

transverse electron oscillations under the off-resonance excitation.

The excitation probability of the dye molecules in the silica shell depends on the relative orientations between the local electric field  $\vec{E}$  and the molecular dipole  $\vec{p}$ . Each nanostructure contains thousands of the dye molecules. If we consider a small volume in the silica shell and assume that the local field in this volume has a given magnitude and direction, an average of  $|\vec{E} \cdot \vec{p}|^2$  over all the possible molecular dipolar orientations gives a result of  $(1/3)(Ep)^2$ . Therefore the fluorescence enhancement factor as defined above will be determined by the ratio of the average electric field intensity enhancement between the longitudinal and transverse polarization excitations. The calculated average electric field intensity enhancement in the silica shell is plotted as a function of the excitation polarization angle in Figure 4b. The field intensity enhancement can be well-fitted with

$$\frac{|\vec{E}|^2}{|\vec{E}_0|^2} = A \cos^2 \theta + B \quad (2)$$

where  $A = 34$ ,  $B = 1.1$ , and  $\theta$  is the excitation polarization angle relative to the nanorod length axis. The small enhancement value of 1.1 calculated under the transversely polarized excitation justifies our above use of the ratio between the maximum and minimum fluorescence intensities as the fluorescence enhancement factor. Moreover, the calculated ratio between the maximum and minimum intensity enhancements is 31.

Previous experiments on plasmon-enhanced fluorescence reveal that both excitation and emission enhancements can contribute to the total fluorescence enhancement on noble metal nanocrystals.<sup>3–8,22</sup> When the localized plasmon resonance wavelength of a metal nanocrystal is close to the excitation wavelength of a fluorescent dye molecule that is placed close to the nanocrystal, the excitation of the molecule will be enhanced due to the local electric field enhancement arising from the plasmon resonance. The excitation enhancement factor  $f_{\text{ex}}$  is proportional to the local field intensity enhancement. When the plasmon resonance wavelength of the nanocrystal is close to the emission wavelength of the molecule, the emission will be enhanced. The emission enhancement is usually thought to take effect as an increase

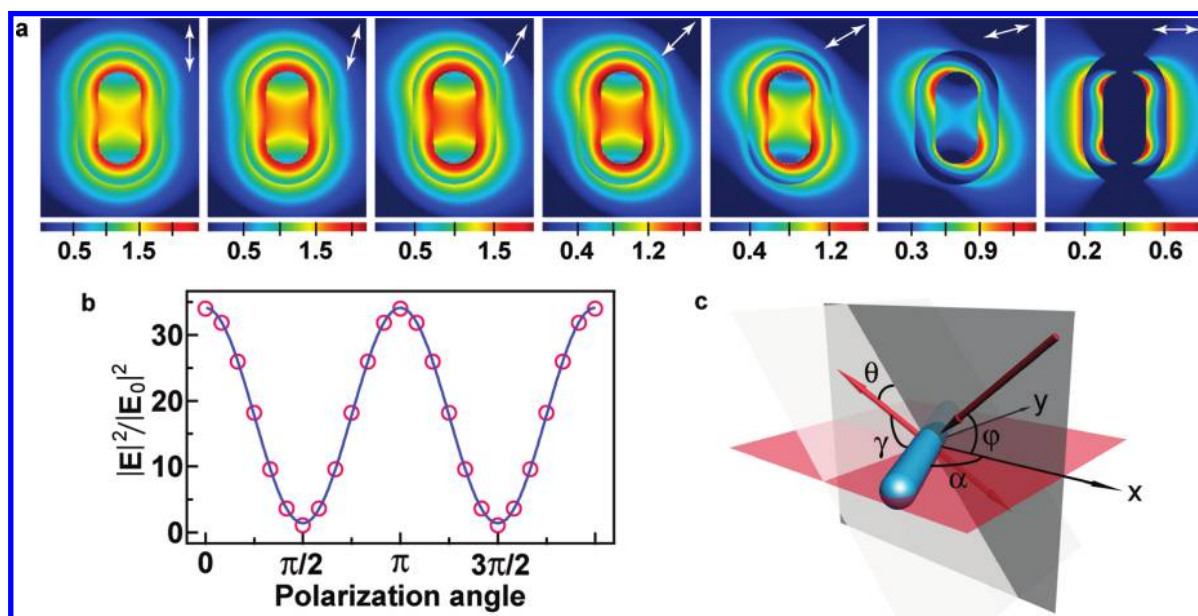


**Figure 4.** Polarization dependence of the average electric field intensity enhancement. (a) Electric field intensity contours obtained from the FDTD calculations on a single core-shell nanostructure. The Au nanorod is oriented vertically. From left to right, the excitation polarization relative to the nanorod length axis is 0°, 15°, 30°, 45°, 60°, 75°, and 90°, respectively. The size is 160 nm × 200 nm for all the contours. The field intensity is at the logarithmic scale. (b) Field intensity enhancement (circles) averaged over the silica shell as a function of the excitation polarization direction. The blue line is a fit. (c) Schematic geometry for the excitation of the plasmon resonance in a nanorod. The nanorod (blue) is in the X–Y plane. The excitation laser beam (red) is in the X–Z plane. The white plane is perpendicular to the excitation laser beam. The white plane and X–Y plane intersect along the Y axis. The double-angled red line is in the white plane. It indicates the polarization direction.

in the radiative decay rate.<sup>32</sup> It can be expressed by  $f_{\text{em}} = \Gamma_r^*/\Gamma_r$ , where  $\Gamma_r^*$  and  $\Gamma_r$  are the radiative decay rates in the presence and absence of the metal, respectively. Because the absorption and emission wavelengths of most organic dyes are close to each other and the plasmon resonance peak widths of noble metal nanocrystals are comparable to the emission peak widths of the dyes, the excitation and emission enhancements usually take effect simultaneously. The total fluorescence enhancement is dependent on the plasmon resonance wavelength relative to the excitation and emission wavelengths and the excitation conditions.

When dye molecules are situated very close to the surface of metal nanocrystals, fluorescence quenching also occurs, which can be taken into account by introducing an additional nonradiative decay with a rate of  $\Gamma_m$ . For the fluorescence quenching on spherical Au nanoparticles, which show small local electric field enhancements, the quenching extent decreases with increasing distances up to 15 nm.<sup>33,34</sup> In contrast, when significant local field enhancements are existent, both the fluorescence quenching and enhancement will take effect. The net result will be determined by the magnitude of the local field enhancement. In fact, net fluorescence enhancements on metal nanocrystals that show large local field enhancements can be observed within much shorter distances, as demonstrated by a recent experiment.<sup>35</sup> In this experiment, a  $\sim 10$  time net fluorescence enhancement is observed when fluorescent dyes are distributed within a shell of 8 nm thickness on gold nanorods. This example suggests that on metal nanocrystals that exhibit large field enhancements, the fluorescence quenching can be overcome by the fluorescence enhancement and a net

fluorescence enhancement can be observed over very small distances.

In our experiments, the excitation light wavelength is fixed at 633 nm by using a laser. However, the emission peak wavelength of oxazine 725 in the hybrid nanostructure is found to shift toward the longitudinal plasmon wavelength in a linear relationship (Figure 3c). According to this linear relationship, when the longitudinal plasmon wavelength of the nanostructure is close to the excitation wavelength and in the range of 635–645 nm, the plasmon resonance peak will nearly overlap with the reshaped emission peak. Therefore in this wavelength region, the total fluorescence enhancement is contributed by both the excitation and emission enhancements and the measured values are 20–60. The abrupt drop in the fluorescence enhancement observed at 620 nm is ascribed to the significant cutoff of the reshaped emission spectra by the long-pass filter. As the longitudinal plasmon wavelength is synthetically tuned to be above 700 nm, the measured enhancement values are below 10. In this wavelength region, the plasmon wavelength is far away from the excitation wavelength but still very close to the emission wavelength due to the spectral reshaping. Therefore the fluorescence enhancement is mainly contributed by the emission enhancement.

The fluorescence intensity of our hybrid nanostructures shows a cosine squared dependence on the excitation polarization direction. The fluorescence enhancement factor  $F$  is determined from the emission intensity ratio between the longitudinal and transverse polarization excitations. It can be determined according to

$$F = \frac{f_{\text{ex},\parallel} \frac{f_{\text{em},\parallel} \Gamma_r}{f_{\text{em},\parallel} \Gamma_r + \Gamma_{\text{nr}} + \Gamma_m}}{f_{\text{ex},\perp} \frac{f_{\text{em},\perp} \Gamma_r}{f_{\text{em},\perp} \Gamma_r + \Gamma_{\text{nr}} + \Gamma_m}} \quad (3)$$

where  $\parallel$  and  $\perp$  represent the longitudinal and transverse polarization excitation, respectively,  $\Gamma_{\text{nr}}$  stands for the nonradiative decay rate. Because the local electric field enhancement under the transverse polarization excitation is very small,  $f_{\text{ex},\perp}$  and  $f_{\text{em},\perp}$  are approximately equal to 1. We therefore have

$$F \approx f_{\text{ex},\parallel} \frac{\frac{f_{\text{em},\parallel} \Gamma_r}{f_{\text{em},\parallel} \Gamma_r + \Gamma_{\text{nr}} + \Gamma_m}}{\Gamma_r} = f_{\text{ex},\parallel} \frac{f_{\text{em},\parallel} \Gamma_r + f_{\text{em},\parallel} \Gamma_{\text{nr}} + f_{\text{em},\parallel} \Gamma_m}{f_{\text{em},\parallel} \Gamma_r + \Gamma_{\text{nr}} + \Gamma_m} \quad (4)$$

The quantum yield of oxazine 725 in ethanol is 0.11.<sup>36</sup> Because its quantum yield is difficult to measure when oxazine 725 is encapsulated in the mesostructured silica, its solution value is taken. The quantum yield of 0.11 indicates that  $\Gamma_{\text{nr}}$  is  $\sim 8$  times of  $\Gamma_r$  and therefore nonnegligible in eq 4.

In our hybrid nanostructures, the dye molecules are distributed in the silica shell of 21 nm thickness. Depending on the sizes of the nanorods, each nanostructure contains about 4000–7000 dye molecules. The measured fluorescence intensity is a sum from all the molecules in the silica shell. Because the local field enhancement is nonuniform around the nanorods and decays exponentially away from the metal surface, the  $f_{\text{ex},\parallel}$ ,  $f_{\text{em},\parallel}$ , and  $\Gamma_m$  for each dye molecule will all change as a function of its spatial position. This complex spatial dependence precludes a quantitative analysis of the fluorescence enhancement on the hybrid nanostructures. However, our FDTD calculations on the representative nanostructure show that the field intensity enhancement averaged over the silica shell also exhibits a cosine squared dependence on the excitation polarization direction. Because both the measured fluorescence intensity and the calculated average field intensity enhancement exhibit the cosine squared dependences, the fluorescence intensity should be proportional to the average field intensity enhancement. This proportionality allows us to make comparison between the measured fluorescence enhancement factor and that obtained from the FDTD calculations. The longitudinal plasmon wavelength of the nanostructure used in the FDTD calculations is 643 nm, and the electric field enhancement contour is calculated at an excitation wavelength of 633 nm. There are six experimental data points within 641–646 nm in Figure 2h. The average fluorescence enhancement factor of these six points is  $29 \pm 9$ . This value is in very good agreement with the calculated value of 31.

The polarization dependence of the fluorescence enhancement allows us to determine the orientation of the individual Au nanorods on substrates. The experimental excitation geometry is schematically shown in Figure 4c. Under the

assumption of a cosine squared dependence on the excitation polarization angle, the relationship between the fluorescence intensity and the excitation polarization angle can be described by (Figure S4 in Supporting Information)

$$\cos \gamma = \sin \alpha \sin \theta + \cos \alpha \sin \varphi \cos \theta \quad (5)$$

$$I = [A(\sin \alpha \sin \theta + \cos \alpha \sin \varphi \cos \theta)^2 + B]e^{-C\theta} \quad (6)$$

where  $A$ ,  $B$ , and  $C$  are constants,  $\gamma$  is the angle between the excitation polarization direction and the nanorod length axis,  $\theta$  is the excitation polarization angle,  $\alpha$  is the orientation angle, and  $\varphi = 40^\circ$  is the laser incidence angle relative to the horizontal plane. The trigonometric term accounts for the cosine squared dependence on the excitation polarization direction. The exponential term accounts for the photobleaching-induced decay. Because the polarization angle is a linear function of time, the exponential term is expressed as a function of the polarization angle. The polarization-dependent fluorescence data for nanostructure 4 can be well-fitted by eq 6 (Figure 2e,f), which proves that our assumption of the cosine squared dependence is correct. The orientation angle of nanostructure 4 obtained from fitting is  $-10^\circ$ . The orientation angle can also be measured under SEM imaging when the substrate is aligned in the same direction as in the optical measurements by the pattern-matching method. The measured angle is  $-9^\circ$  (Figure 2a). The two values are nearly the same. We also determined the orientation angles of the other nanostructures in Figure 2a by fitting their polarization-dependent fluorescence data (Figure S5 in Supporting Information). The obtained values are  $-49^\circ$ ,  $-2^\circ$ ,  $30^\circ$ ,  $-33^\circ$ , and  $42^\circ$  for the nanostructures 2, 3, 5, 6, and 7, respectively. For comparison, the corresponding values measured from SEM imaging are  $-55^\circ$ ,  $-1^\circ$ ,  $35^\circ$ ,  $-35^\circ$ , and  $42^\circ$ , respectively. The fluorescence intensity of nanostructure 1 is much weaker. Its fluorescence data were not analyzed.

The polarization dependence of the plasmon-enhanced fluorescence was further demonstrated on the single Au nanorods that are embedded in oxazine 725-incorporated mesostructured silica thin films (Figure 5a,b). The mesostructured silica thin films containing the Au nanorods and oxazine 725 were fabricated on cleaned glass slides using dip coating.<sup>37</sup> Before coating, 1 mL of the as-prepared Au nanorod dispersion was centrifuged at 6000 rpm for 10 min and redispersed in 3 mL of water. Glass slides were immersed in the obtained nanorod solution for 5 min, rinsed with water, and then blown dry with nitrogen. The silica precursor solution was prepared by mixing 1.04 g of tetraethyl orthosilicate with 0.8 g of ethanol and 0.54 g of water (pH = 2.0, prepared with HCl) and stirring the mixture for 20 min. Separately, 0.28 g of (ethylene oxide)<sub>20</sub>–(propylene oxide)<sub>70</sub>–(ethylene oxide)<sub>20</sub> triblock copolymer was dissolved in 11.1 g of ethanol. The two solutions were mixed, 6.4 mg of oxazine 725 was added, and the resultant mixture was stirred for 2–3 h at room temperature before coating. Mesostructured silica thin films were dip-coated on the Au nanorod-deposited glass slides at a speed of 1 cm min<sup>-1</sup>. The films were dried in air



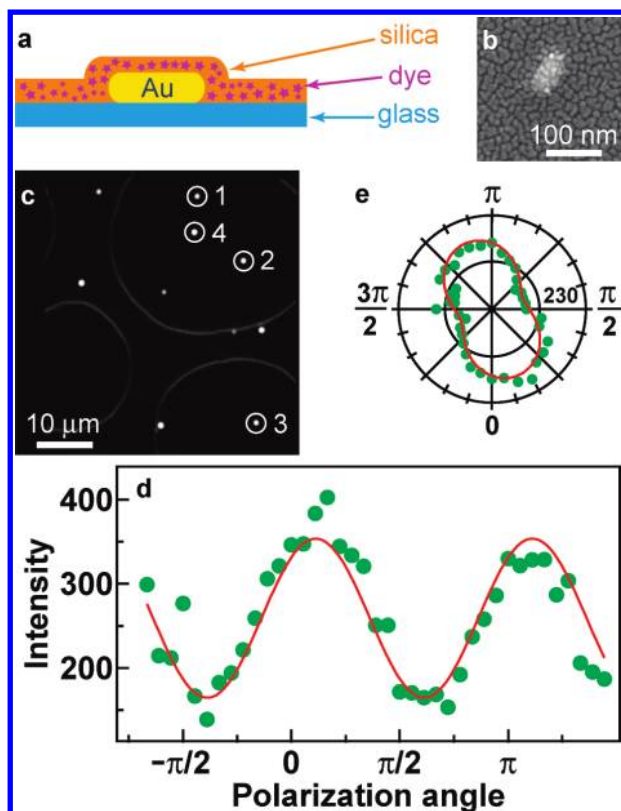


**Figure 5.** Polarization dependence of the plasmon-enhanced fluorescence on the single Au nanorods that are incorporated in mesostructured silica thin films. (a) Schematic illustration of the hybrid thin films composed of the Au nanorods, mesostructured silica, and oxazine 725. (b) SEM image of a single Au nanorod embedded in a mesostructured silica thin film. The film was sputter-coated with gold. (c) Scattering image of several Au nanorods embedded in a mesostructured silica thin film. The numbers indicate the nanorods on which the polarization dependence of the plasmon-enhanced fluorescence was measured. The large circles result from scattering at the steps on the film. (d) Dependence of the fluorescence intensity on the excitation polarization angle (solid green circles) for the nanorod 2. The red curve is a fit to a cosine squared function. (e) Polar plot of the fluorescence intensity (solid green circles) versus the excitation polarization direction. The red curve is drawn according to the fitted one in d.

overnight before optical measurements. The thicknesses of the films were measured on a Tencor Alpha-Step 500 surface profiler to be 32–48 nm. The individual Au nanorods are clearly visible under dark-field imaging (Figure 5c). For each bright spot on the scattering image, there is a corresponding bright spot on the fluorescence image. Its emission intensity varies with the excitation polarization direction (Figure 5d,e and Figure S6 in Supporting Information). Fitting the emission intensity points with eq 6 gives the fluorescence enhancement factors and the orientation angles of the Au nanorods. The obtained fluorescence enhancement factors for the four labeled nanorods shown in Figure 5c are 2.1, 3.6, 3.7, and 1.8, and their orientation angles are  $51^\circ$ ,  $13^\circ$ ,  $-30^\circ$ , and  $37^\circ$ , respectively. The reduction in the fluorescence enhancement factor is due to oxazine 725 molecules distributed within the entire silica film. Many molecules are far away from any Au nanorod, but their fluorescence is collected under both longitudinally and transversely polarized excitations.

In conclusion, a strong polarization dependence of plasmon-enhanced fluorescence has been observed on individual Au nanorods that are coated with or embedded in a fluorophore-incorporated mesostructured silica layer. The polarization dependence is ascribed to the dependence of the averaged electric field intensity enhancement around the individual gold nanorods on the excitation polarization direction. The maximum fluorescence enhancement occurs when the longitudinal plasmon wavelength of the Au nanorods is nearly equal to the excitation laser wavelength. The shaping of the emission spectra of the fluorophores by the longitudinal plasmon mode of the individual Au nanorods has also been shown. We have further demonstrated the determination of the orientation angle of the Au nanorods on substrates on the basis of the polarization dependence.

**Acknowledgment.** We are grateful for financial support of this work from National Natural Science Foundation of China (Project Code: 20828001), CUHK Block Grant (Reference: 5/06C-SF, Project Code: 3110023), and RGC Research Grant Direct Allocation (Project Code: 2060358).

**Supporting Information Available:** Growth of the Au nanorods, derivation of the dependence of the fluorescence intensity on the excitation polarization, the absorption and emission spectra of oxazine 725, the extinction spectra of the Au nanorods, two-dimensional Gaussian fit, the polarization dependence of the plasmon-enhanced fluorescence on the Au nanorod–silica shell hybrid nanostructures and the Au nanorods embedded in the mesostructured silica thin film. This material is available free of charge via the Internet at <http://pubs.acs.org>.

## References

- (1) Graham, D.; Thompson, D. G.; Smith, W. E.; Faulds, K. *Nat. Nanotechnol.* **2008**, *3*, 548–551.
- (2) Pompa, P. P.; Martiradonna, L.; Della Torre, A.; Della Sala, F.; Manna, L.; de Vittorio, M.; Calabi, F.; Cingolani, R.; Rinaldi, R. *Nat. Nanotechnol.* **2006**, *1*, 126–130.
- (3) Kühn, S.; Håkanson, U.; Rogobete, L.; Sandoghdar, V. *Phys. Rev. Lett.* **2006**, *97*, 017402.
- (4) Chen, Y.; Munechika, K.; Ginger, D. S. *Nano Lett.* **2007**, *7*, 690–696.
- (5) Zhang, J.; Fu, Y.; Chowdhury, M. H.; Lakowicz, J. R. *Nano Lett.* **2007**, *7*, 2101–2107.
- (6) Muskens, O. L.; Giannini, V.; Sánchez-Gil, J. A.; Rivas, J. G. *Nano Lett.* **2007**, *7*, 2871–2875.
- (7) Chen, Y.; Munechika, K.; Plante, I. J.-L.; Munro, A. M.; Skrabalak, S. E.; Xia, Y. N.; Ginger, D. S. *Appl. Phys. Lett.* **2008**, *93*, 053106.
- (8) Wang, Y. K.; Yang, T. Y.; Tuominen, M. T.; Achermann, M. *Phys. Rev. Lett.* **2009**, *102*, 163001.
- (9) Kim, S.; Jin, J.; Kim, Y.-J.; Park, I.-Y.; Kim, Y.; Kim, S.-W. *Nature* **2008**, *453*, 757–760.
- (10) Jain, P. K.; Xiao, Y. H.; Walsworth, R.; Cohen, A. E. *Nano Lett.* **2009**, *9*, 1644–1650.
- (11) Sundararajan, S. P.; Grady, N. K.; Mirin, N.; Halas, N. J. *Nano Lett.* **2008**, *8*, 624–630.
- (12) Sundaramurthy, A.; Schuck, P. J.; Conley, N. R.; Fromm, D. P.; Kino, G. S.; Moerner, W. E. *Nano Lett.* **2006**, *6*, 355–360.
- (13) Lee, J.-S.; Shevchenko, E. V.; Talapin, D. V. *J. Am. Chem. Soc.* **2008**, *130*, 9673–9675.
- (14) Lieberman, I.; Shemer, G.; Fried, T.; Kosower, E. M.; Markovich, G. *Angew. Chem., Int. Ed.* **2008**, *47*, 4855–4857.
- (15) Sönnichsen, C.; Alivisatos, A. P. *Nano Lett.* **2006**, *5*, 301–304.
- (16) Moerland, R. J.; Taminiau, T. H.; Novotny, L.; van Hulst, N. F.; Kuipers, L. *Nano Lett.* **2008**, *8*, 606–610.
- (17) Schubert, O.; Becker, J.; Carbone, L.; Khalavka, Y.; Provalska, T.; Zins, I.; Sönnichsen, C. *Nano Lett.* **2008**, *8*, 2345–2350.



- (18) Taminiau, T. H.; Stefani, F. D.; van Hulst, N. F. *New J. Phys.* **2008**, *10*, 105005.
- (19) Zijlstra, P.; Chon, J. W. M.; Gu, M. *Nature* **2009**, *459*, 410–413.
- (20) Mertens, H.; Biteen, J. S.; Atwater, H. A.; Polman, A. *Nano Lett.* **2006**, *6*, 2622–2625.
- (21) McLellan, J. M.; Li, Z.-Y.; Siekkinen, A. R.; Xia, Y. N. *Nano Lett.* **2007**, *7*, 1013–1017.
- (22) Bek, A.; Jansen, R.; Ringler, M.; Mayilo, S.; Klar, T. A.; Feldmann, J. *Nano Lett.* **2008**, *8*, 485–490.
- (23) Wei, H.; Hao, F.; Huang, Y. Z.; Wang, W. Z.; Nordlander, P.; Xu, H. X. *Nano Lett.* **2008**, *8*, 2497–2502.
- (24) Lee, S. J.; Baik, J. M.; Moskovits, M. *Nano Lett.* **2008**, *8*, 3244–3247.
- (25) Shegai, T.; Li, Z. P.; Dadosh, T.; Zhang, Z. Y.; Xu, H. X.; Haran, G. *Proc. Natl. Acad. Sci. U.S.A.* **2008**, *105*, 16448–16453.
- (26) Ni, W. H.; Kou, X. S.; Yang, Z.; Wang, J. F. *ACS Nano* **2008**, *2*, 677–686.
- (27) Tsung, C.-K.; Kou, X. S.; Shi, Q. H.; Zhang, J. P.; Yeung, M. H.; Wang, J. F.; Stucky, G. D. *J. Am. Chem. Soc.* **2006**, *128*, 5352–5353.
- (28) Gorelikov, I.; Matsuura, N. *Nano Lett.* **2008**, *8*, 369–373.
- (29) Wang, J. F.; Tsung, C.-K.; Hong, W. B.; Wu, Y. Y.; Tang, J.; Stucky, G. D. *Chem. Mater.* **2004**, *16*, 5169–5181.
- (30) Bakker, R. M.; Yuan, H.-K.; Liu, Z. T.; Drachev, V. P.; Kildishev, A. V.; Shalaev, V. M.; Pedersen, R. H.; Gresillon, S.; Boltasseva, A. *Appl. Phys. Lett.* **2008**, *92*, 043101.
- (31) Ringler, M.; Schwemer, A.; Wunderlich, M.; Nichtl, A.; Kürzinger, K.; Klar, T. A.; Feldmann, J. *Phys. Rev. Lett.* **2008**, *100*, 203002.
- (32) Liu, N. G.; Prall, B. S.; Klimov, V. I. *J. Am. Chem. Soc.* **2006**, *128*, 15362–15363.
- (33) Dulkeith, E.; Ringler, M.; Klar, T. A.; Feldman, J.; Javier, A. M.; Parak, W. J. *Nano Lett.* **2005**, *5*, 585–589.
- (34) Schneider, G.; Decher, G.; Nerambourg, N.; Praho, R.; Werts, M. H. V.; Blanchard-Desce, M. *Nano Lett.* **2006**, *6*, 530–536.
- (35) Bardhan, R.; Grady, N. K.; Cole, J. R.; Joshi, A.; Halas, N. J. *ACS Nano* **2009**, *3*, 744–752.
- (36) Sens, R.; Drexhage, K. H. *J. Lumin.* **1981**, *24/25*, 709–712.
- (37) Wang, J. F.; Stucky, G. D. *Adv. Funct. Mater.* **2004**, *14*, 409–415.

NL902095Q

# Strong Polarization Dependence of Plasmon-Enhanced Fluorescence on Single Gold Nanorods

Tian Ming, Lei Zhao, Zhi Yang, Huanjun Chen, Lingdong Sun, Jianfang Wang,\* and Chunhua Yan

Department of Physics, the Chinese University of Hong Kong, Shatin, Hong Kong SAR, and State Key

Lab of Rare Earth Materials Chemistry and Applications, Peking University, Beijing 100871, China

## Supporting Information

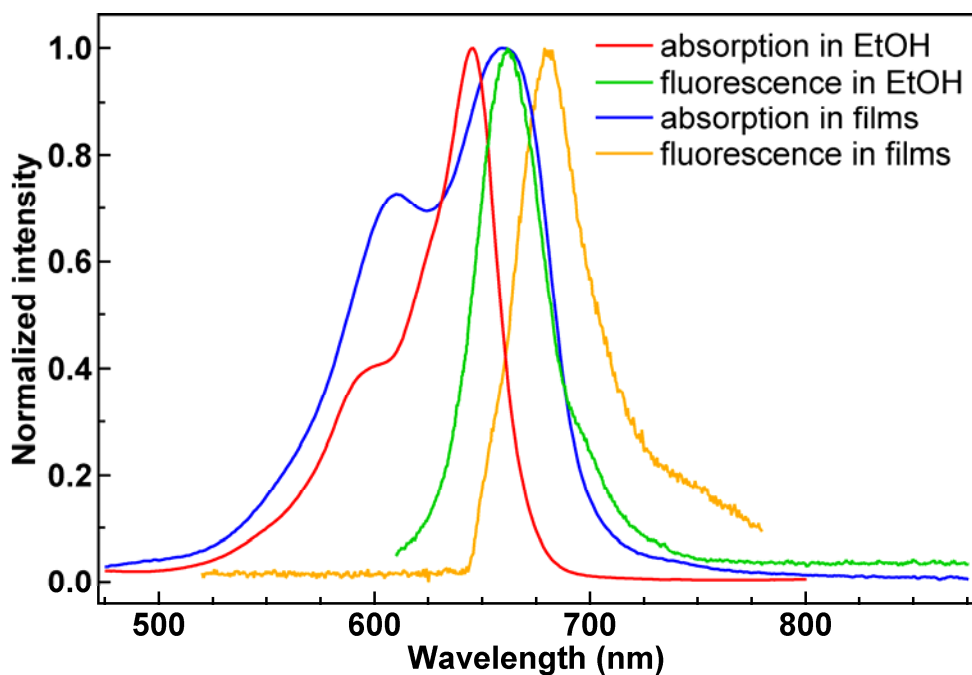


**Figure S1.** Absorption and emission spectra of oxazine 725. When dissolved in ethanol, the dye has a major absorption peak at 645 nm and a minor absorption peak at 600 nm (red curve). Its maximum emission wavelength is 662 nm (green curve). When the dye is embedded in mesostructured silica, its major and minor absorption peaks are red-shifted to 660 and 610 nm, respectively (blue curve). Its emission peak is red-shifted by 20 nm (orange curve). Absorption spectra of solution samples were recorded on a Hitachi U-3501 UV–visible–NIR spectrophotometer. Fluorescence emission spectra of solution samples were taken on a Hitachi F-4500 spectrofluorometer.

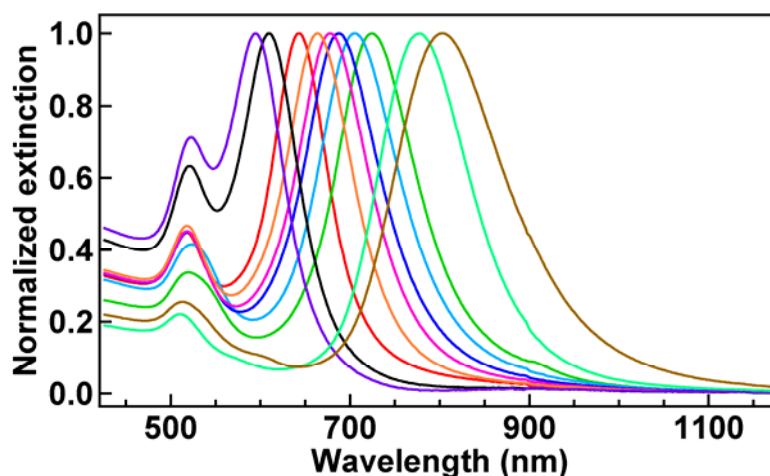


**Figure S2.** Extinction spectra of Au nanorods. Au nanorods are stabilized with CTAB molecules and dispersed in aqueous solutions. Their longitudinal plasmon resonance wavelengths from left to right are 594, 610, 646, 664, 678, 688, 706, 726, 778, and 802 nm, respectively. The growth of these Au nanorods is described below. Extinction spectra of solution samples were recorded on a Hitachi U-3501 UV–visible–NIR spectrophotometer.

The Au nanorods were grown using a seed-mediated method. Their longitudinal plasmon wavelengths were finely controlled through an anisotropic oxidation reaction. Among the nanorods shown in Figure S2, those with longitudinal plasmon wavelengths of 726 and 802 nm were grown through the seed-mediated method. For the growth of the Au nanorods with a longitudinal plasmon wavelength of 726 nm, the seed solution was prepared by the addition of a freshly prepared, ice-cold aqueous  $\text{NaBH}_4$  solution (0.01 M, 0.6 mL) into an aqueous mixture solution composed of  $\text{HAuCl}_4$  (0.01 M, 0.25 mL) and CTAB (0.1 M, 9.75 mL). The resultant solution was mixed by rapid inversion for 2 min and then kept at room temperature for at least 2 h before use. The growth solution was made by first mixing together aqueous solutions of  $\text{HAuCl}_4$  (0.01 M, 2 mL),  $\text{AgNO}_3$  (0.01 M, 0.4 mL), and CTAB (0.1 M, 40 mL). A freshly prepared aqueous ascorbic acid solution (0.1 M, 0.32 mL) was then added, followed by the addition of an aqueous HCl solution (1.0 M, 0.8 mL). After the resultant solution was mixed by inversion, the seed solution (0.01 mL) was then added. The reaction mixture was



subjected to gentle inversion for 10 s and then left undisturbed for at least 6 h. The preparation of the Au nanorods with a longitudinal plasmon wavelength of 802 nm followed the same procedure, except that the volume of the seed solution was increased to 0.02 mL. The Au nanorods with longitudinal plasmon wavelengths of 706, 688, 678, 664, 646, 610, and 594 nm were produced by anisotropic oxidation of the nanorod sample with a longitudinal plasmon wavelength of 726 nm. The Au nanorods with a longitudinal plasmon wavelength of 778 nm were obtained from anisotropic oxidation of the nanorod sample with a longitudinal plasmon wavelength of 802 nm. For oxidation, an aqueous HCl solution (1.0 M, 0.2 mL) was added in the as-grown Au nanorod solution (10 mL), followed by bubbling O<sub>2</sub> into the mixture solution for 1 min. The mixture solution was kept uncapped in an isothermal oven at 65 °C for 2–25 h. The longitudinal plasmon wavelength of the Au nanorods became shorter with increasing oxidation time. After oxidation, the Au nanorods were precipitated by centrifugation and then re-dispersed in 0.1 M aqueous CTAB solutions at the same volume.

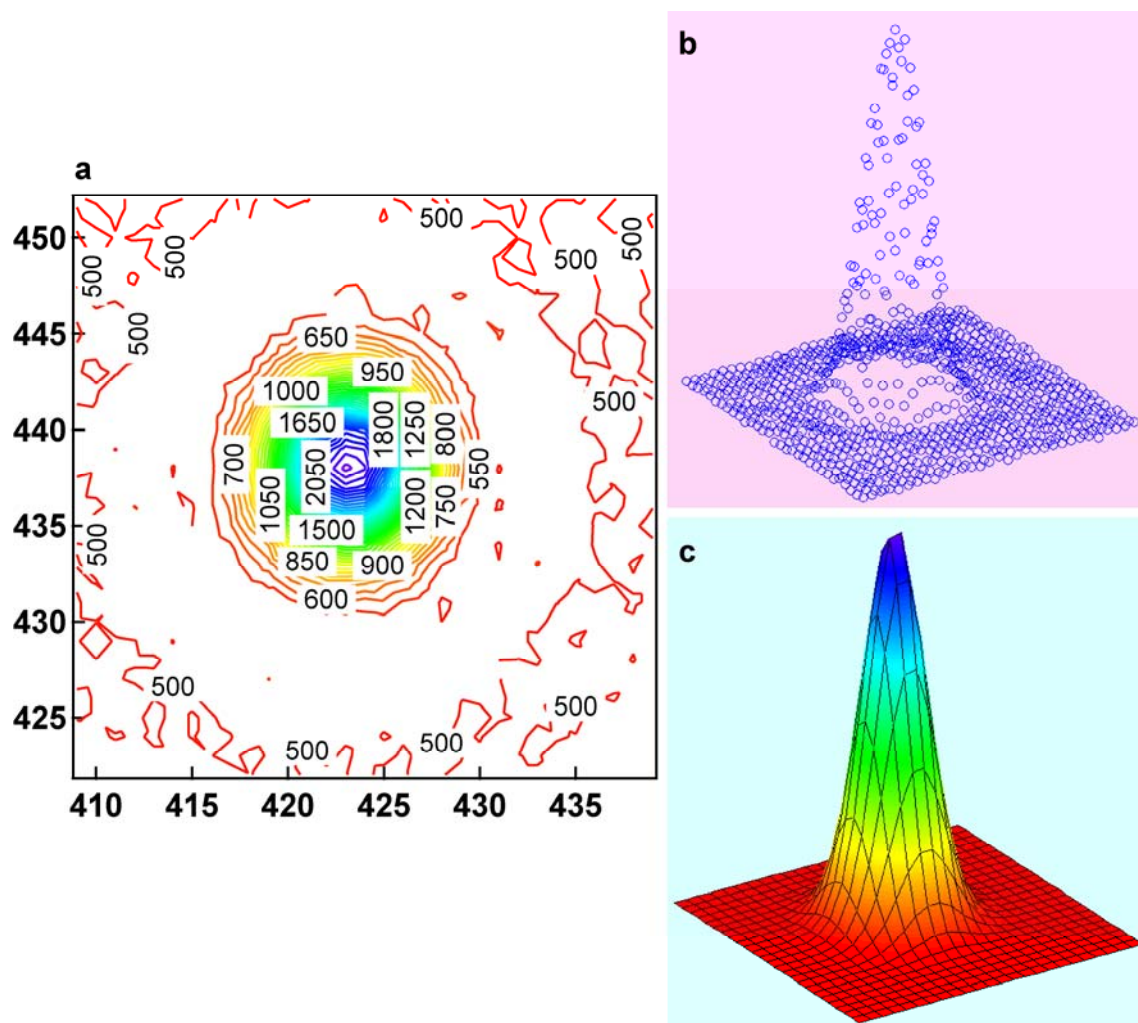


**Figure S3.** Determination of fluorescence peak intensities. (a) Contour plot of a typical fluorescence spot taken out of a fluorescence image. The two axes represent pixel numbers. The numbers in the plot are fluorescence intensities. The size of the region is  $31 \times 31$  pixels, corresponding to  $3.1 \mu\text{m} \times 3.1 \mu\text{m}$ . (b) Surface plot of the fluorescence peak. (c) Surface plot obtained from two-dimensional Gaussian fitting. The peak value is taken as the fluorescence intensity of the spot.

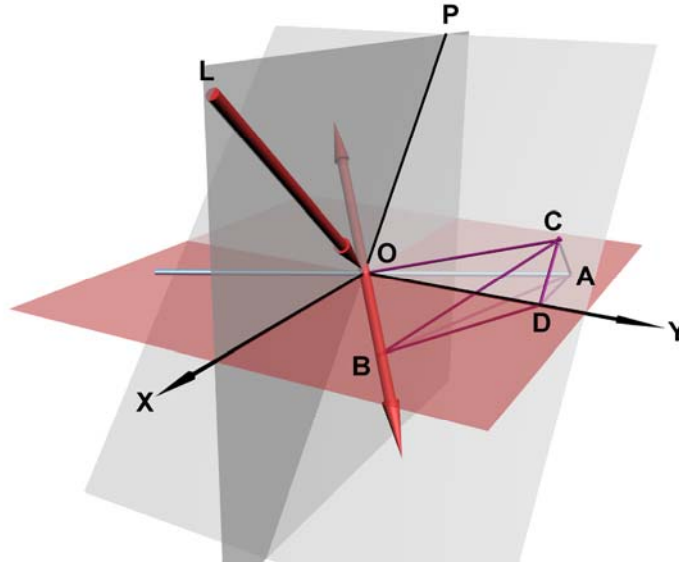


**Figure S4.** Schematic geometry for the excitation of the plasmon mode of a nanorod. The derivation of the dependence of the projected electric field component along the length axis of the nanorod on the polarization angle of the excitation laser light is described below.

The nanorod (light blue) lies in the X-Y plane. The excitation laser light (red) is in the X-Z plane. The white plane is perpendicular to the excitation light. The intersection line between the white plane and X-Z plane is used as a reference line for the polarization direction of the excitation light. The double-headed red line represents the polarization direction of the excitation light.

For derivation, a line perpendicular to the white plane is drawn from one end of the nanorod A. The intersection point between this line and the white plane is C. A line is then drawn from the origin O to the point C. Two more lines are drawn from the point C. One is perpendicular to the polarization direction and intersects with it at the point B. The other is perpendicular to the Y axis and intersects with it at the point D.

Because  $AC \perp OB$  and  $BC \perp OB$ , therefore  $OB \perp \Delta ABC$ . Then we have  $OB \perp AB$ .  $\Delta AOB$ ,  $\Delta BOC$ , and  $\Delta AOC$  are all right triangles. We then have

$$\cos \angle AOB = \frac{OB}{OA}, \cos \angle BOC = \frac{OB}{OC}, \cos \angle AOC = \frac{OC}{OA}.$$

Therefore,



$$(\cos \angle AOC)(\cos \angle BOC) = \cos \angle AOB.$$

Because  $AC \perp OY$  and  $CD \perp OY$ , therefore  $OY \perp \Delta ACD$ . Then we have  $AD \perp OY$ . Therefore  $AD \parallel OX$ .

We have  $\angle AOX = \angle OAD$ . Because  $OL \parallel AC$ , therefore  $\angle LOX = \angle CAD$ . Because

$$\cos \angle CAD = \frac{AC}{AD}, \cos \angle OAD = \frac{AD}{OA}, \sin \angle AOC = \sin\left(\frac{\pi}{2} - \angle OAC\right) = \cos \angle OAC = \frac{AC}{OA},$$

therefore

$$(\cos \angle CAD)(\cos \angle OAD) = \sin \angle AOC.$$

Because

$$\frac{\pi}{2} = \angle BOP + \angle BOC + \angle COD,$$

therefore

$$\cos \angle BOC = \sin(\angle BOP + \angle COD).$$

Because

$$\cos \angle AOC = \frac{OC}{OA}, \cos \angle COD = \frac{OD}{OC}, \sin \angle AOX = \sin\left(\frac{\pi}{2} - \angle AOD\right) = \cos \angle AOD = \frac{OD}{OA},$$

therefore

$$(\cos \angle AOC)(\cos \angle COD) = \sin \angle AOX.$$

From the above equations, we then have

$$\begin{aligned} \cos \angle AOB &= (\cos \angle AOC)(\cos \angle BOC) \\ &= (\cos \angle AOC)\sin(\angle BOP + \angle COD) \\ &= (\cos \angle AOC)[(\sin \angle BOP)(\cos \angle COD) + (\cos \angle BOP)(\sin \angle COD)] \\ &= (\cos \angle AOC)(\cos \angle COD)(\sin \angle BOP) + (\cos \angle BOP)(\sin \angle COD)(\cos \angle AOC) \\ &= (\sin \angle AOX)(\sin \angle BOP) + (\cos \angle BOP)\sqrt{1 - (\cos \angle COD)^2}(\cos \angle AOC)^2 \\ &= (\sin \angle AOX)(\sin \angle BOP) + (\cos \angle BOP)\sqrt{(\cos \angle AOC)^2 - (\sin \angle AOX)^2}. \end{aligned}$$

The term under the square root can be converted to

$$\begin{aligned} (\cos \angle AOC)^2 - (\sin \angle AOX)^2 &= 1 - (\sin \angle AOC)^2 - (\sin \angle AOX)^2 \\ &= 1 - (\cos \angle CAD)^2(\cos \angle OAD)^2 - (\sin \angle AOX)^2 \\ &= (\cos \angle AOX)^2 - (\cos \angle CAD)^2(\cos \angle AOX)^2 \\ &= (\cos \angle AOX)^2(\sin \angle LOX)^2. \end{aligned}$$

We then obtain

$$\cos \angle AOB = (\sin \angle AOX)(\sin \angle BOP) + (\cos \angle BOP)(\cos \angle AOX)(\sin \angle LOX).$$

If we let the angle between the polarization direction and the nanorod  $\angle AOB = \gamma$ , the polarization angle  $\angle BOP = \theta$ , the orientation angle of the nanorod  $\angle AOX = \alpha$ , and the incidence angle of the excitation light  $\angle LOX = \varphi$ , then

$$\cos \gamma = \sin \alpha \sin \theta + \sin \varphi \cos \alpha \cos \theta .$$

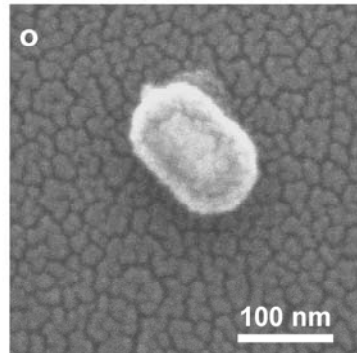
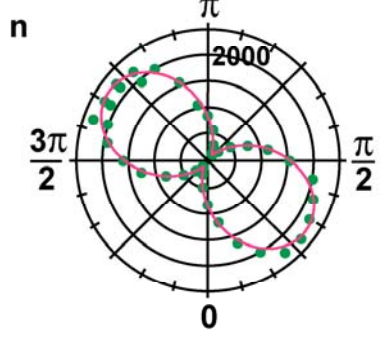
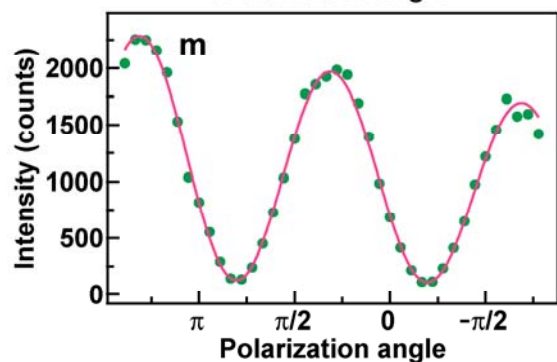
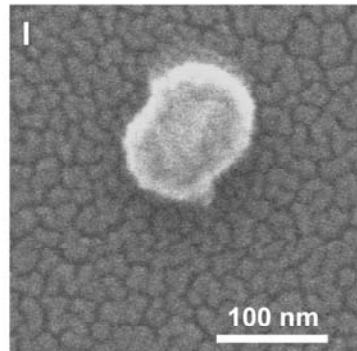
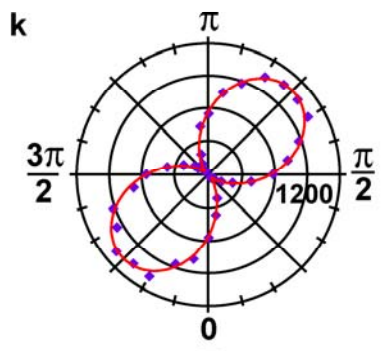
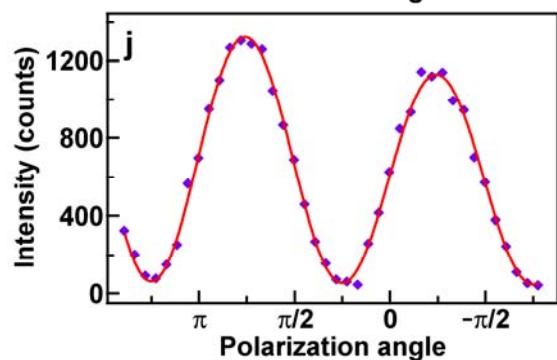
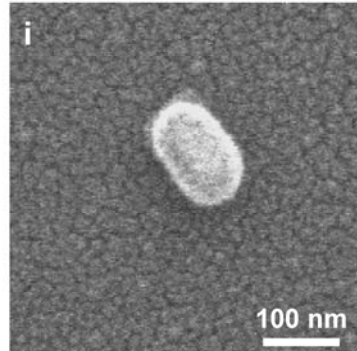
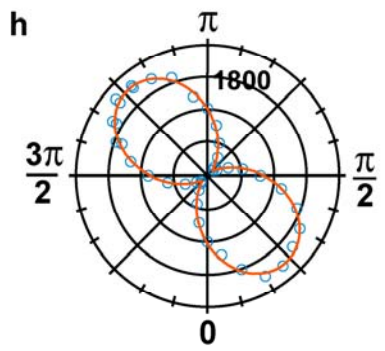
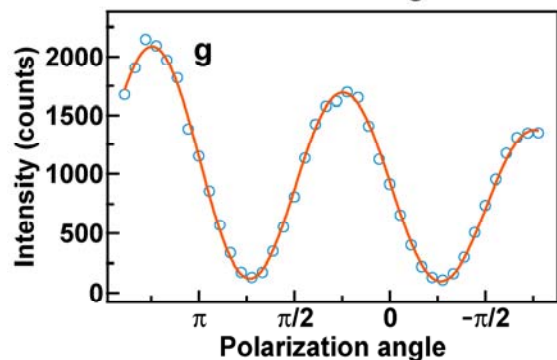
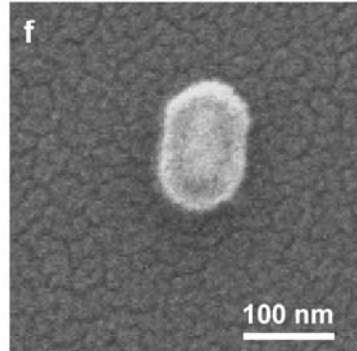
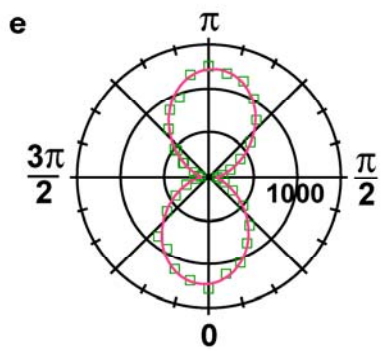
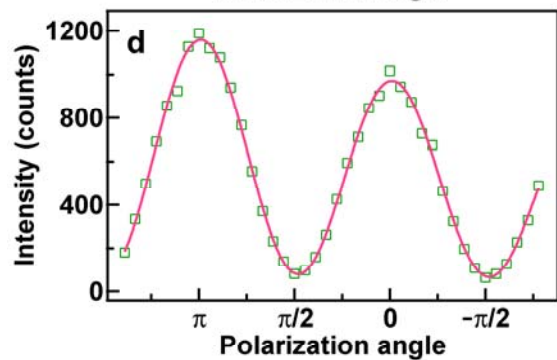
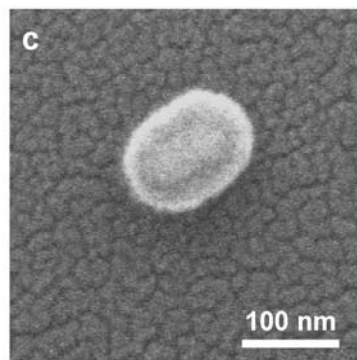
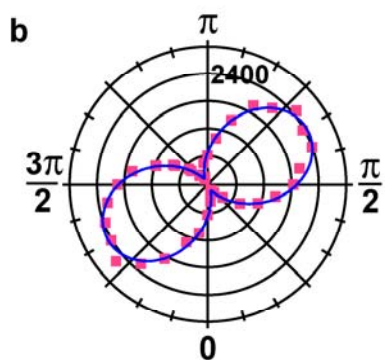
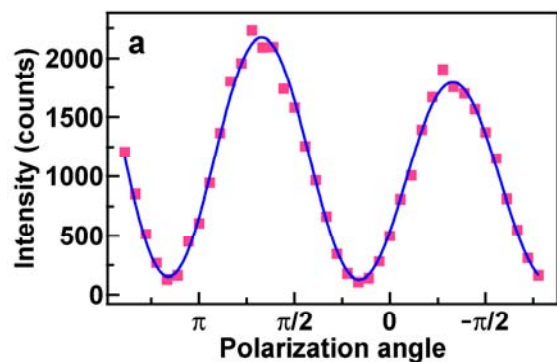




**Figure S5.** Polarization dependence of plasmon-enhanced fluorescence on single Au nanorods. (a) Variation of the fluorescence intensity (solid red squares) as a function of the excitation polarization angle for the nanostructure 2 shown in Figure 2a. The blue curve is a fit. (b) Polar plot of the dependence of the fluorescence intensity (solid red squares) on the excitation polarization direction. The blue curve is drawn according to the fitted one in a. (c) SEM image of the nanostructure 2. (d–f) For the nanostructure 3 shown in Figure 2a. (g–i) For the nanostructure 5 shown in Figure 2a. (j–l) For the nanostructure 6 shown in Figure 2a. (m–o) For the nanostructure 7 shown in Figure 2a. The fluorescence intensity decay owing to photobleaching has been removed from the polar plots.

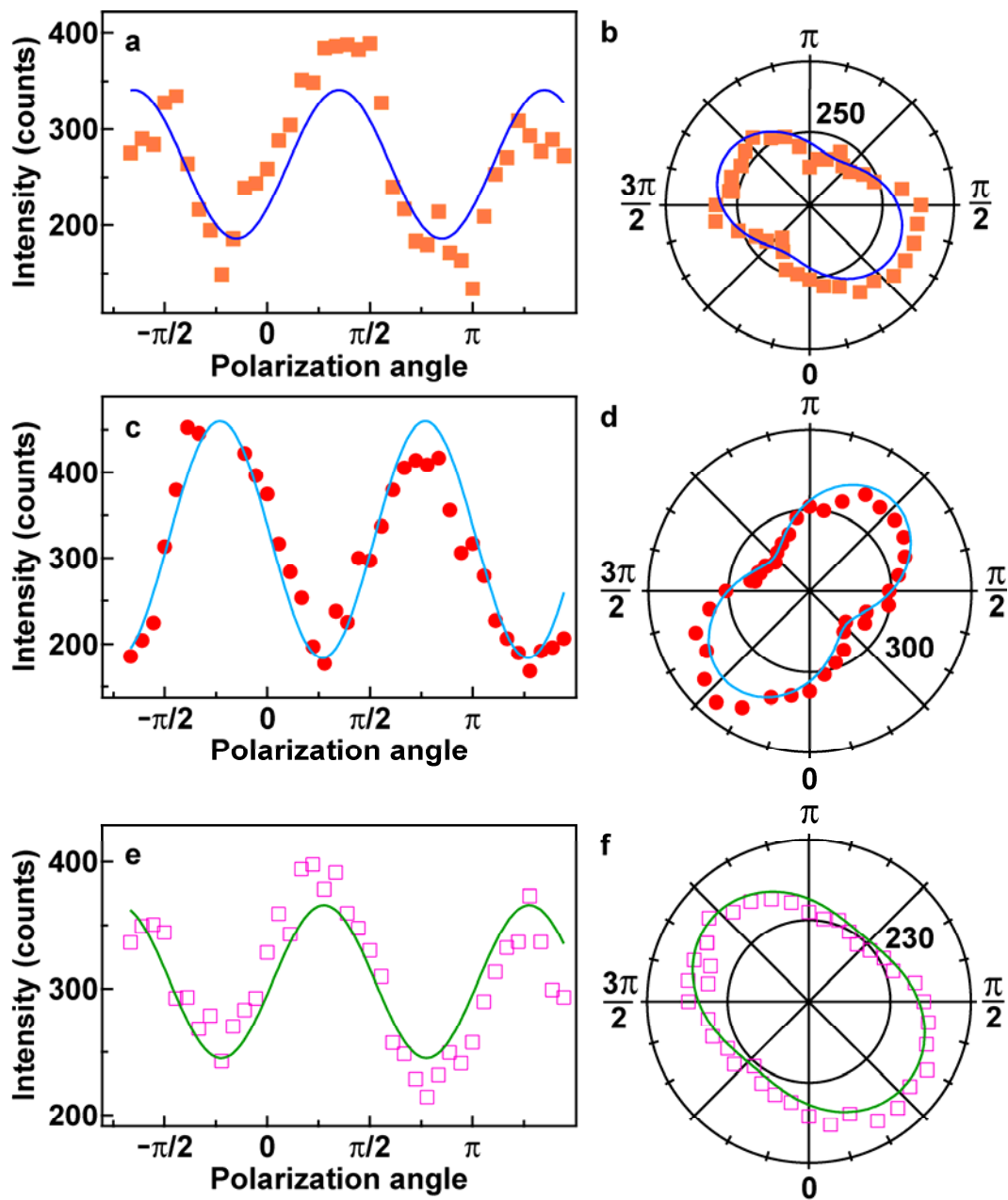


**Figure S6.** Polarization dependence of plasmon-enhanced fluorescence on single Au nanorods that are embedded in mesostructured silica thin films. (a) Variation of the fluorescence intensity (solid orange squares) as a function of the excitation polarization angle for the nanorod 1 shown in Figure 5c. (b) Polar plot of the fluorescence intensity (solid orange squares) versus the polarization angle. The blue curve is drawn according to the fitted one in a. (c,d) For the nanorod 3 shown in Figure 5c. (e,f) For the nanorod 4 shown in Figure 5c.